Co-doped willemite ceramic pigments: Technological behaviour, crystal structure and optical properties

Emel Ozel [a], Hilmi Yurdakul [a], Servet Turan [a], Matteo Ardit [b,*],
Giuseppe Cruciani [b], Michele Dondi [c]

[a] *Department of Materials Science and Engineering, Anadolu University, İki Eylül Campus, 26480 Eskişehir, Turkey*
[b] *Department of Earth Sciences, University of Ferrara, Via Saragat 1, 44100 Ferrara, Italy*
[c] *Institute of Science and Technology for Ceramics (ISTEC-CNR), Via Granarolo 64, 48018 Faenza, Italy*

Abstract

Cobalt-doped willemite is a promising blue ceramic pigment, but some important aspects concerning crystal structure, optical properties and technological behaviour are still undisclosed. In order to get new insight on these features, willemite pigments ($Zn_{2-x}Co_xSiO_4$, $0 < x < 0.3$) were synthesized by the ceramic route and characterized from the structural (XRPD with Rietveld refinement), optical (DRS and colorimetry), microstructural (SEM, STEM, TEM, EDX, EELS) and technological (simulation of the ceramic process) viewpoints. The incorporation of cobalt in the willemite lattice, taking preferentially place in the Zn1 tetrahedral site, induces an increase of unit-cell parameters, metal–oxygen distances, and inter-tetrahedral tilting. It causes shifting and enhanced splitting of spin-allowed bands of Co^{2+} in tetrahedral coordination, implying slight changes of crystal field strength Dq and Racah B parameter, but increasing spin-orbit coupling parameter λ. Willemite pigments impart deep blue hue to ceramic glazes and glassy coatings with a colouring performance better than commercial Co-bearing colorants in the 800–1200 °C range. Detailed SEM-TEM investigation and microanalysis proved that no diffusion phenomena occur at the pigment–glassy coating interface and that willemite pigments are chemically inert during firing at 1050 °C.
© 2010 Elsevier Ltd. All rights reserved.

Keywords: Electron microscopy; Spectroscopy; X-ray methods; Optical properties; Willemite

1. Introduction

Willemite, Zn_2SiO_4 (trigonal, R-3H) with phenakite structure is an orthosilicate with all atoms in general position and composed by a framework of tetrahedra accommodating zinc and silicon in three different fourfold crystallographic sites: two slightly different zinc sites Zn1 ($\langle Zn–O \rangle$ 1.950 Å) and Zn2 ($\langle Zn–O \rangle$ 1.961 Å), and Si ($\langle Si–O \rangle$ 1.635 Å), so resulting in rhombohedral symmetry with lattice parameters $a = b \sim 13.948$ Å, and $c \sim 9.315$ Å.[1–4]

Such a rigid lattice, with only non-centrosymmetric cationic sites, gives the chance to get special optical properties; in fact, synthetic willemite is meeting an increasing interest for its potential as phosphor host (e.g. with Eu^{3+}, Mn^{2+}, Tb^{3+}, Ce^{3+}

doping),[5–10] glass–ceramics,[11,12] dielectric ceramics for wireless applications,[13] and it has been proposed, because of its high-temperature stability, as ceramic pigment.[14–16] As in the case of the well-known spinel pigments $(Zn,Co)Al_2O_4$ (DCMA 13-26-2 and 13-28-2), a deep blue colour is obtained by doping the willemite structure with cobalt, that replaces zinc ions in tetrahedral positions. The advantage of willemite pigments comes from suitably saturated hues that can be obtained with a lower Co amount with respect to spinel $CoAl_2O_4$ or olivine $(Co_2SiO_4$, DCMA 5-08-2) colorants.[15]

In this study, production and characterization of willemite ceramic pigments, obtained by using ZnO powders which are industrial by-products, were undertaken. Different pigment compositions, having $Zn_{2-x}Co_xSiO_4$ stoichiometry (where $0 < x < 0.3$), were designed and synthesized in order to get a new insight into the interrelationships between crystal structure, coloration and technological behaviour. In particular, structural features (XRD), optical properties (DRS) and thermal stabil-

Table 1

Chemical composition of raw materials used in pigment preparation. The chemical composition of raw materials (Co_3O_4 and ZnO) were determined by X-ray fluorescence spectrometer (XRF, Rigaku RZS Primus).

wt%	ZnO (from slag)	Co_3O_4 (Ferro)	SiO_2 (Riedel-de Haen)	ZnO (Fluka)
ZnO	95.5	–	–	≥99.0%
Co_3O_4	–	96.7	–	–
PbO	1.62	–	–	–
NiO	0.02	–	–	–
CuO	0.53	–	–	–
Fe_2O_3	0.14	0.053	–	–
Al_2O_3	–	0.105	–	–
CaO	0.07	0.024	–	–
K_2O	0.25	–	–	–
Na_2O	–	1.49	–	–
MgO	–	0.034	–	–
SiO_2	0.12	0.043	≥98.0%	–
SO_3	1.74	1.56		

ity and pigment–glaze interactions (SEM, TEM, EELS) were appraised investigating the $Zn_{2-x}Co_xSiO_4$ join before the transition to the olivine structure-type.

2. Experimental procedure

2.1. Sample preparation

Reagent grade SiO_2 (Riedel-de Haën) and Co_3O_4 (Ferro) plus ZnO from industrial metal slag were used as raw materials (Table 1). No mineralizer was added.

All pigment compositions were designed and prepared according to the following stoichiometry:

$$Zn_{2-x}Co_xSiO_4$$

where $x = 0$, 0.05, 0.1, 0.2, and 0.3. Prepared pigment compositions were labeled as WX and given in Table 3. X represents the Co content in the pigment composition.

The pigments were synthesized by the conventional ceramic process: wet mixing of raw materials, drying in oven, pulverization in agate mortar, then calcination in alumina crucible in an electric kiln in static air at maximum temperature of 1300 °C for 3 h (heating rate of 2 °C/min, natural cooling). Furthermore, a reference sample (Zn_2SiO_4) was synthesized entirely from pure raw materials.

2.2. X-ray powder diffraction (XRPD) and structural characterisation

X-ray powder measurements were performed using a D8 Advance (Bruker, Karlsruhe, Germany) equipped with a Si(Li) solid-state detector, set to acquire Cu $K\alpha_1/K\alpha_2$ radiation. Scans were recorded in the 15–130° 2θ range, with a counting time of 10 s per 0.02° 2θ step.

The structural refinements were performed by the Rietveld method using the GSAS-EXPGUI software packages.[17,18] The diffraction peak profiles were modelled by a pseudo-Voigt

Table 2

Chemical composition and main physical features of glazes and glassy coatings used in technological tests.

| Component/property	Unit	Glassy coatings				Glazes			
		F1	F2	F3	F4	S1	S2	S3	S4
SiO_2	wt%	63.9	57.1	62.9	49.3	53.5	51.1	49.7	61.3
ZrO_2		<0.1	<0.1	0.2	0.2	<0.1	<0.1	8.1	6.0
B_2O_3		11.7	8.9	11.8	19.8	<0.1	1.2	2.4	<0.1
Al_2O_3		9.5	9.0	10.7	3.3	25.2	22.6	19.7	11.2
MgO		<0.1	1.1	0.2	0.3	3.4	1.4	0.2	1.1
CaO		0.5	7.9	2.9	2.5	8.9	13.5	12.6	9.9
ZnO		1.0	5.0	2.5	6.0	<0.1	5.1	<0.1	0.2
BaO		<0.1	1.4	2.8	9.2	<0.1	1.4	3.2	<0.1
PbO		5.5	2.7	0.2	0.8	<0.1	0.9	<0.1	<0.1
Li_2O		<0.1	<0.1	<0.1	2.0	<0.1	<0.1	<0.1	0.1
Na_2O		6.1	2.0	2.7	5.1	5.6	2.6	2.2	3.4
K_2O		1.1	4.1	2.6	1.1	3.0	0.6	1.3	0.4
Crystalline phases after firing	wt%	<10	5–15	<10	<10	10–20	40–50	10–20	5–15
Softening temperature[a]	°C	930	940	910	720	1210	1150	1100	1210
Temperature of half sphere[a]	°C	1265	1180	1240	820	1275	1200	1195	1300
Coeff. thermal expansion $\alpha_{20-400\,°C}$	MK^{-1}	4.96	5.59	4.55	6.07	6.83	5.54	4.97	5.62

[a] Determined by hot-stage microscopy.
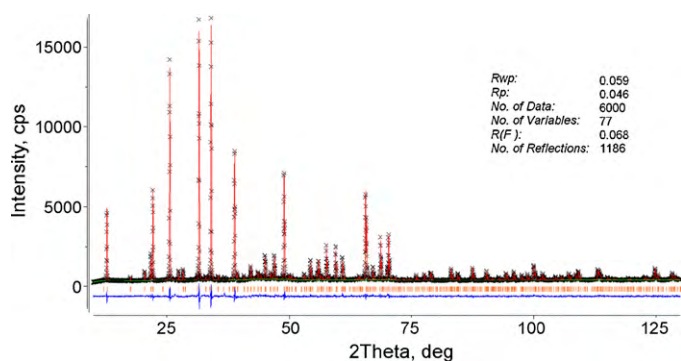
Fig. 1. Plot of Rietveld refinement performed on X-ray powder diffraction data of sample W30. The experimental data are indicated by cross signs, the calculated pattern is the continuous line and the lower curve is the weighted difference between the calculated and observed patterns. The rows of vertical tick marks shows the allowed reflections for the crystalline phase present in the sample.

function with one Gaussian and two Lorentzian broadening coefficients plus an asymmetry contribution. Besides the shifted Chebyshev polynomial coefficients to reproduce the background, all refinements included a scale factor, the profile coefficients and the cell parameters. The willemite structure refinement was carried out in the R-3H space group, starting from the model of McMurdie and co-workers.[4] A typical Rietveld plot is reported for un-doped willemite (sample W30) in Fig. 1.

2.3. UV–vis-NIR diffuse reflectance spectroscopy (DRS)

Electron absorption spectroscopy was performed by diffuse reflectance (λ19 spectrophotometer, Perkin Elmer, Waltham, MS) using 300–2450 nm range, 0.1 nm step size, 480 nm/min scan rate, $BaSO_4$ integrating sphere and $BaSO_4$ white reference material. Reflectance (R_∞) was converted to absorbance (K/S) by the Kubelka–Munk equation: $K/S = 2/(1 - R_\infty) \cdot (2R_\infty)^{-1}$, which accounts for absorption (K) and scattering (S).[20] Absorbance bands (Gaussian) were deconvoluted (PFM, OriginLab, Northampton, MA) in order to obtain energy (peak centroid) with good fitting ($X^2 < 1\%$) and an experimental error, including background correction and reproducibility, around 2%. Crystal field strength $10Dq$ and interelectronic repulsion Racah parameter B were calculated by fitting the mean energy of spin-allowed transitions in the Tanabe-Sugano diagram for d^7 ions in tetrahedral coordination (the same of d^3 in sixfold coordination).[21,22] The spin-orbit coupling parameter λ was calculated fitting the energy of sub-bands of the threefold split $^4T_1(^4P)$ transition.[21]

2.4. Technological performance

Technological performance of willemite pigments was evaluated by adding 5 wt% of pigment W30 into different types of glassy coatings (i.e. frit giving rise to a transparent coating) and glazes (i.e. mix of frit and minerals giving rise to an opaque vitro-crystalline coating) for ceramic tiles and sanitaryware (Table 2).[23,24] Every batch was wet mixed and the slip sprinkled on porous ceramic tiles, then dried in oven and fired
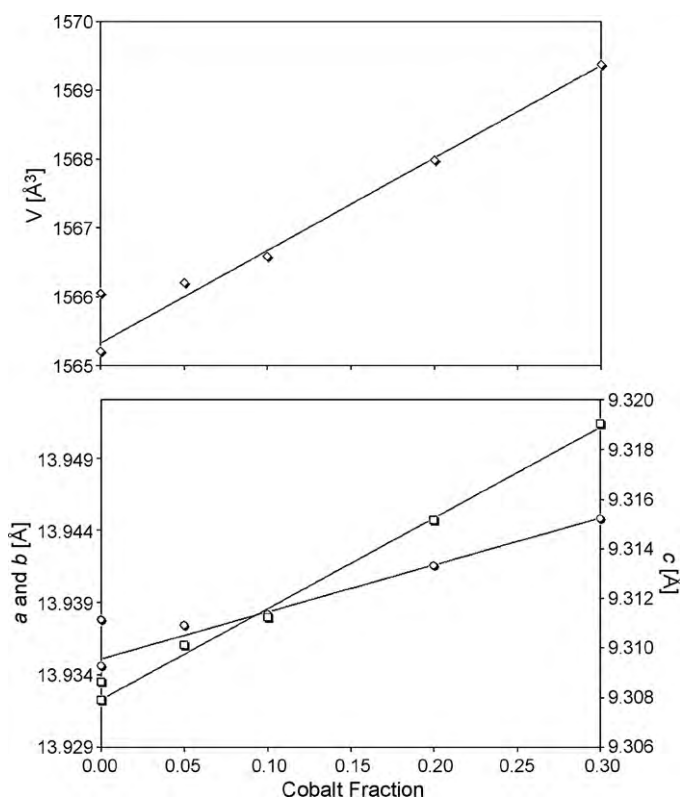

Fig. 2. Unit-cell volume (V: diamonds) and lattice parameters ($a = b$: circles; c: squares) of willemite pigments as a function of cobalt doping (white symbols); reference sample WR (grey symbols).

with different schedules in electric roller kiln (800–1200 °C, 1 h cold-to-cold) or chamber furnace (1250 °C, 12 h cold-to-cold). The colour stability was evaluated by measuring the CIELab parameters of coatings by MSXP4000 Miniscan spectrometer (Hunterlab, white glazed tile reference $x = 31.5$, $y = 33.3$, illuminant D_{65}, 10° observer). The colouring performance of willemite pigment was compared with commercial Co-olivine and Co-aluminate colorants, that were added taking care that the Co amount be the same in all glazes/glassy coatings.

2.5. Pigment–coating interactions

In order to evaluate its chemical stability, the W30 Co-willemite pigment was admixed to glassy coating F1 and fired at 1050 °C with dwell time of 30 min. The pigment was selected since it has the most intense blue colour and the coating was selected since it contains the lowest amount of ZnO among the compositions here considered. Samples were polished with cross section polisher (Jeol SM-09010, Japan) for scanning electron microscope (SEM) examinations (Zeiss, Supra 50 VP, Germany). Focus ion beam lift out method (FEI-Nova 600 NanoLab DualBeam^{TM}, USA) was used for transmission electron microscope (TEM) sample preparation. Electron transparent samples were characterised by using 200 kV field emission TEM (Jeol 2100F, Japan) attached with an energy filter (Gatan GIF Tridiem), parallel electron energy loss spectrometer (PEELS), a high angle annular dark field scanning transmission electron

microscope (STEM-HAADF) detector (Fishione) and an energy dispersive X-ray (EDX) spectrometer (Jeol JED-2300T, Japan). In the STEM-EDX/EELS analysis, an electron spot with 1–2 nm in diameter was used and the acquisition time was chosen as 40-s live time. Furthermore, a drift corrector was used to avoid any possible drifts that may occur at nano-scale during acquisition of STEM-EDX spot and line scan elemental analysis. In STEM-EELS analysis, the convergence and collection semi-angles were 9.2 and 15.7 mrad, respectively. The spectrometer energy dispersions were 0.2 and 0.5 eV/channels. The backgrounds of all acquired EEL and reference spectra were subtracted according to power-law in this study.[25]

3. Results and discussion

3.1. Crystal structure

In our synthesis conditions, the major phase occurring in all samples is willemite plus a small amount of residual phases due to the low purity ZnO raw material.

The incorporation of cobalt in the willemite lattice is clearly proved by the increase of the unit-cell parameters and volume, proportional to the cobalt doping (Fig. 2). This fact is unexpected on the basis of ionic radii (Zn^{2+} 0.60 Å, Co^{2+} 0.58 Å, in tetrahedral coordination) but is readily explained by a varying covalency degree of the M–O bonding. In fact, it is known that the Zn–O bonding exhibits an enhanced covalency, due to the strong hybridization of sp^3 orbitals, that promotes particularly short Zn–O distances.[26] The result of the Co → Zn substitution implies a more ionic bond and longer M–O distance.

Doping up to 0.1 apfu produces small crystal structural changes, but appreciable increasing of unit-cell volume occurs for Co additions ≥0.2 apfu (Fig. 2).

Nevertheless, the refined mean ⟨Zn1–O⟩ and ⟨Zn2–O⟩ distances, even with a narrow range of variation, suggest that cobalt takes place in both Zn1 and Zn2 sites, but with a different preference: an expansion can be recognized for the Zn1 tetrahedron (the one with originally shorter distances), while the Zn2 tetrahedron remains constant or slightly contracts (Table 3). As reported for different doping of the willemite structure, ions with smaller ionic radii should be hosted in the smaller zinc cation site.[3,10,27,28] On this basis, Co^{2+} is expected to be mainly hosted in the Zn1 sites (average polyhedral volume = 3.770 Å^3) with a maximum tetrahedral deviation δ(Zn1–O) = 0.018 Å, while zinc atoms should be preferentially placed on the Zn2 site (average polyhedral volume = 3.910 Å^3) with a smaller tetrahedral deviation δ(Zn2–O) = 0.006 Å (Fig. 3).

Another important evidence, indicating the mechanism of cobalt incorporation in the willemite tetrahedral sites, stems from inter-tetrahedral tilting. The analysis of variance among the three T–O–T angles hinged on each oxygen site shows that the tetrahedral tilting mostly involves the O4 and O3 hinges. The T–O4–T angles become more dissimilar with increasing Co content, while the opposite occurs for the T–O3–T angles. This means that the tilting arrangement around the O3 and O4 hinges are made progressively less equivalent by the Co substitution (Fig. 4).
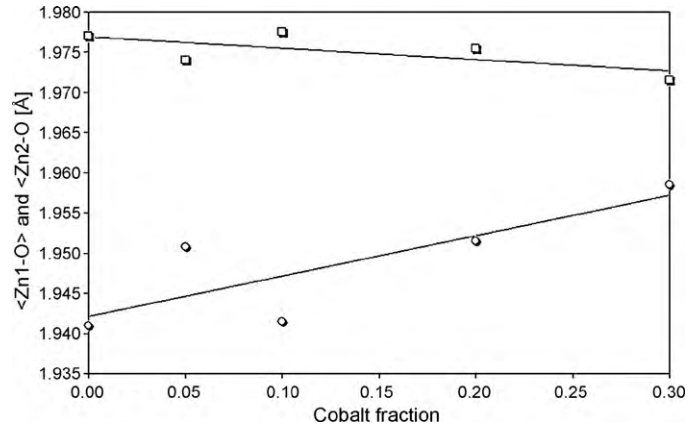

Fig. 3. Mean metal–oxygen distances in the tetrahedral sites Zn1 (circles) and Zn2 (squares) of willemite pigments as a function of cobalt doping.
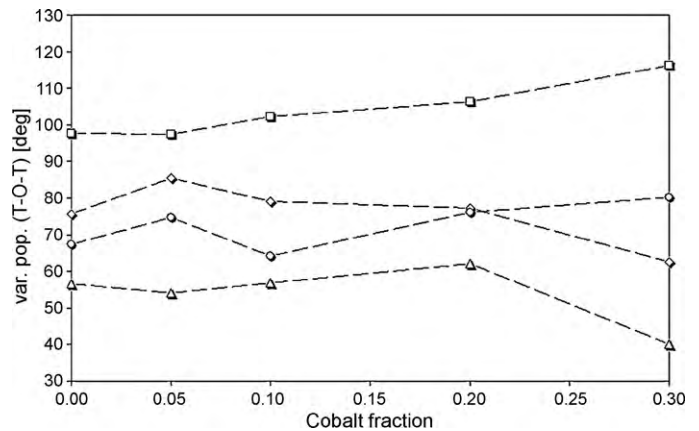

Fig. 4. Variance of T–O–T angles in willemite pigments as a function of cobalt doping: T–O1–T (diamond), T–O2–T (circle), T–O3–T (triangle), T–O4–T (square).

3.2. Optical properties

The optical spectra of cobalt-bearing willemite pigments are characterized by electron transitions of Co^{2+} in tetrahedral coordination (Fig. 5) which exhibit increasing absorbance values matching fairly well with the nominal cobalt occupan-
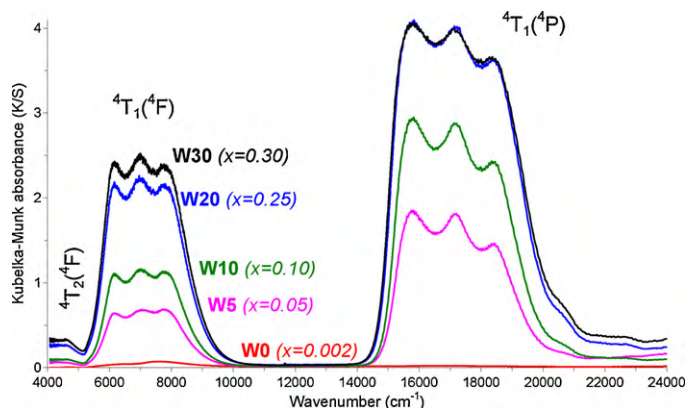

Fig. 5. Optical spectra of cobalt-bearing willemite pigments (x = cobalt content, apfu).

Table 3
Batch composition, X-ray diffraction details, unit-cell parameters, metal–oxygen distances, effective volume and T–O–T angles in willemite structures analyzed.

Sample label	WR	W0	W5	W10	W20	W30
Nominal cobalt content						
$Zn_{2-x}Co_xSiO_4$; $x=$	0.00	0.00	0.05	0.10	0.20	0.30
Agreement factors and refinement details						
R_{wp}	0.1242	0.0812	0.0630	0.0442	0.0294	0.0592
R_p	0.0818	0.0520	0.0411	0.0297	0.0213	0.0455
No. of data	6250	6000	6000	6000	6000	6000
$R_F{}^2$	0.0427	0.0378	0.0457	0.0490	0.0545	0.0679
No. of reflections	1184	1184	1184	1186	1186	1186
No. of variables	77	77	77	77	77	77
Unit-cell parameters ($\alpha = \beta = 90°$; $\gamma = 120°$)						
$a = b$ (Å)	13.9378(1)	13.9346(1)	13.9374(1)	13.9382(1)	13.9415(1)	13.9448(1)
c (Å)	9.30867(1)	9.30791(1)	9.31012(1)	9.31125(1)	9.31514(1)	9.31903(1)
Unit-cell volume (Å³)	1566.05	1565.21	1566.21	1566.58	1567.98	1569.37
Tetrahedral metal–oxygen mean distances (Å)						
Zn1–O	1.956	1.941	1.951	1.942	1.952	1.959
Zn2–O	1.971	1.977	1.974	1.978	1.976	1.972
Si–O	1.620	1.626	1.620	1.627	1.620	1.619
Polyhedral volume (Å³)						
Zn1	3.81	3.72	3.77	3.72	3.77	3.82
Zn2	3.90	3.92	3.90	3.92	3.91	3.90
Si	2.18	2.20	2.18	2.20	2.18	2.17
T–O–T angles						
Zn2–O1–Zn2	108.6(5)	110.5(6)	109.5(6)	110.0(7)	110.0(6)	109.3(5)
Zn2–O1–Si	131.5(7)	131.5(8)	132.0(9)	131.6(10)	131.4(10)	128.2(8)
Zn2–O1–Si	119.9(7)	117.9(8)	118.5(9)	118.3(10)	118.6(10)	122.4(9)
Av.	120.0	120.0	120.0	120.0	120.0	120.0
Variance	87.4	75.6	85.5	79.1	77.3	62.5
Zn1–O2–Zn1	109.9(6)	110.4(7)	110.4(8)	111.0(8)	111.0(7)	110.6(6)
Zn1–O2–Si	132.1(8)	130.4(9)	131.3(10)	130.4(11)	131.7(11)	132.0(9)
Zn1–O2–Si	118.0(7)	118.6(8)	117.9(9)	118.1(10)	116.8(10)	117.1(9)
Av.	120.0	119.8	119.9	119.8	119.8	119.9
Variance	84.1	67.4	74.7	64.2	76.0	80.2
Zn1–O3–Zn2	112.4(5)	110.5(5)	110.3(5)	110.3(6)	109.6(6)	111.2(6)
Zn1–O3–Si	127.4(7)	128.9(7)	128.1(8)	128.7(9)	128.7(10)	126.0(10)
Zn2–O3–Si	120.2(7)	120.5(8)	121.5(8)	120.8(9)	121.5(10)	122.6(10)
Av.	120.0	120.0	120.0	119.9	119.9	119.9
Variance	37.5	56.6	54.0	56.8	62.0	40.1
Zn1–O4–Zn2	105.0(4)	105.9(4)	106.1(4)	105.8(5)	105.4(4)	104.6(5)
Zn1–O4–Si	128.4(10)	129.1(10)	129.5(13)	129.9(11)	129.5(11)	129.9(9)
Zn2–O4–Si	123.5(10)	123.5(10)	123.1(12)	122.8(11)	124.0(11)	123.8(9)
Av.	119.0	119.5	119.6	119.5	119.6	119.4
Variance	101.5	97.7	97.5	102.2	106.3	116.2

Note: Figures in parentheses are standard deviations in the last decimal figure. The polyhedral volume is calculated as reported by Swanson and Peterson.[19] The variance of the T–O–T angles is defined by $\sum (x - \bar{x})^2 / n$, where x is the mean value of the sample average and n is the sample dimension.

cies. Sample W0, even if nominally Co-free, in reality contains cobalt traces as low as $x = 0.002$ (likely due to contamination in unsealed crucible).

The spectra are dominated by the spin-allowed, threefold split $^4T_1(^4F) \leftarrow {}^4A_2(^4F)$ and $^4T_1(^4P) \leftarrow {}^4A_2(^4F)$ transitions, occurring at about 6000–8000 and 16,000–18,500 cm^{-1}, respectively, together with the low intensity band around 4600 cm^{-1} attributable to the $^4T_2(^4F) \leftarrow {}^4A_2(^4F)$ transition (Fig. 5).

The $^4T_2(^4F)$ transition was fitted with a single band (Fig. 6(a)). The $^4T_1(^4F)$ triple band is almost symmetrical (Fig. 6(b)) and was easily deconvoluted in three components ($^4A_2$, $^4A_2$, $^4A_2$) originating by the splitting due to both low point symmetry of tetrahedral sites in willemite and spin-orbit coupling of Co^{2+} ions.[10,22,29] Deconvolution of the complex band

at 16,000–18,500 cm^{-1} (Fig. 6(c)) required five peaks: the main three are attributed to splitting of the $^4T_1(^4P)$ transition ($^4A_2$, $^4B_{1/2}$, $^4B_{2/1}$). The others are likely due to spin-forbidden transitions, four of which originate from the ^2G term and are expected to occur, according to the Tanabe-Sugano diagram built with the experimental 10Dq and B values, around ~16,200 cm^{-1} (^2E), ~16,900 cm^{-1} ($^2T_1$), ~18,400 cm^{-1} ($^2A_1$) and ~19,400 cm^{-1} ($^2T_2$).

The Co^{2+} spin-allowed transitions exhibit a progressive shift toward lower energy with increasing cobalt content, particularly evident for the $^4T_2$ and $^4T_1(^4P)$ bands (Table 4 and Fig. 7(a)). The crystal field strength Dq and Racah B parameter are nearly constant around $Dq = 398$ cm^{-1} and $B = 810$ cm^{-1} (Fig. 7(b)); these values are close to willemite with Co doping as low as

Table 4
Optical properties of willemite pigments.

Sample			W0	W5	W10	W20	W30
Co concentration (x)			(0.002)	0.05	0.10	0.20	0.30
Spin-allowed transitions		SFT[a]	cm^{-1}	cm^{-1}	cm^{-1}	cm^{-1}	cm^{-1}
T_d symmetry	C_v symm.						
$^4T_2$ (^4F)	$^4A_2$		4750	4610	4605	4600	4595
	$^4A_2$		5700	6150	6150	6130	6120
$^4T_1$ (^4F)	$^4A_2$		6300	6880	6880	6870	6870
	$^4A_2$		7500	7720	7750	7750	7750
		^2E		15,520	15,450	15,340	15,280
	$^4A_2$	$^2T_1$	15,300	16,130	16,050	15,950	15,880
$^4T_1$ (^4P)	$^4B_{1/2}$		17,000	17,210	17,160	17,060	17,000
	$^4B_{2/1}$	$^2A_1$	18,700	18,350	18,390	18,440	18,450
		$^2T_2$		20,500	20,500	20,530	20,590
$^4T_1$ (^4F) band mean energy				6500	6917	6927	6917	6913
$^4T_1$ (^4P) band mean energy			17,000	17,230	17,200	17,150	17,110
$^4T_1$ (^4F) band splitting (δ)			1800	1570	1600	1620	1630
$^4T_1$ (^4P) band splitting (δ)			3400	2220	2340	2490	2570
Crystal field strength (Dq)			475	461	460.5	460	459
Racah B parameter			680	747	747	739	742
Racah C parameter			2720	2988	2988	2956	2968

[a] Spin-forbidden transitions.

0.01 apfu ($Dq = 404$ cm^{-1} and $B = 792$ cm^{-1}).[10] This implies that little changes of covalency degree and Co–O local distance occur going toward the Co end-member. However, the increase of the $^4T_1$ band splitting and spin-orbit parameter λ, occurring in the same direction, confirms the change in the local symmetry of ligands observed by XRD in terms of O–Co–O angles (Fig. 7(c)).

3.3. Technological behaviour of willemite pigments

Co-doped willemite behaves successfully in the ceramic process, imparting intense blue colour to various glazes and glassy coatings. When compared with commercial Co-aluminate and Co-olivine colorants, willemite pigments exhibit similar trends in function of coating composition and firing temperature, but present the best colouring performance in the 800–1200 °C range, as shown by the best value of the parameter b^* (Fig. 8). The strong blue shade of willemite implies a characteristic colour, that is as saturated as that of cobalt aluminate, but less saturated than that of cobalt silicate, as shown by the lower value of L^*. These results strengthen previous indications on the technological behaviour of willemite pigments.[15,16]

The thermal stability of both willemite and commercial pigments appears to be reduced in high-temperature glazes. Passing from 1100 °C to over 1200 °C, willemite pigments become gradually less blue, as a consequence of the converging action of increasing firing temperature and aggressive chemical environments due to high concentration of calcium, magnesium and zinc in molten glazes (for example S1 composition).

3.4. Pigment–coating interactions

In order to assess the chemical stability of Co-willemite pigments, backscattered images of W30 particles dispersed in the glassy coating F1 were taken at high magnification under SEM

Table 5
Chemical composition (wt%) of willemite pigment dispersed in glassy coating (see Fig. 9(a) for the localization of analyzed points).

	Glassy coating Point 1	Pigment Point 2	Pigment Point 3
SiO$_2$	63.36	46.70	40.89
Al$_2$O$_3$	9.29	6.08	5.20
CaO	1.52	0.65	0.64
CoO	2.00	4.95	6.43
ZnO	13.49	31.83	38.48
PbO	4.04	1.67	1.26
Na$_2$O	5.07	7.65	6.72
K$_2$O	1.23	0.48	0.43

and composition of elements in pigment particles were determined by line scan EDX analysis (Fig. 9). The absence of image contrast indicates that there is no reaction layer between the pigment particle and the matrix within the resolution limit of SEM (Fig. 9(a)). Looking at the line scan analysis, the Ca, K and Pb concentration is almost the same in both pigment and glass, implying that a diffusion of Ca and K occurred from glass to willemite; Co and Zn amounts seem to decrease when the edge of the pigment grain is reached (Fig. 9(b)). Spot analysis at different points, shown in Fig. 9(a), partially confirms that glass contains Zn and Co, likely diffusing from the pigment particle (Table 5), but a certain effect of electron beam broadening during EDX analysis cannot be ruled out. Therefore, TEM is needed to go in depth in the pigment–glass interactions during firing at 1050 °C (Fig. 10). The whole length size of sample prepared with focused ion beam technique was approximately 15 μm × 6 μm, which was limited to only the glass region around one single pigment particle to avoid underneath grain effect causing misleading results in chemical analysis.[30] Prior to chemical analysis, STEM-HAADF imaging technique was carried out to highlight any chemical contrast to assess
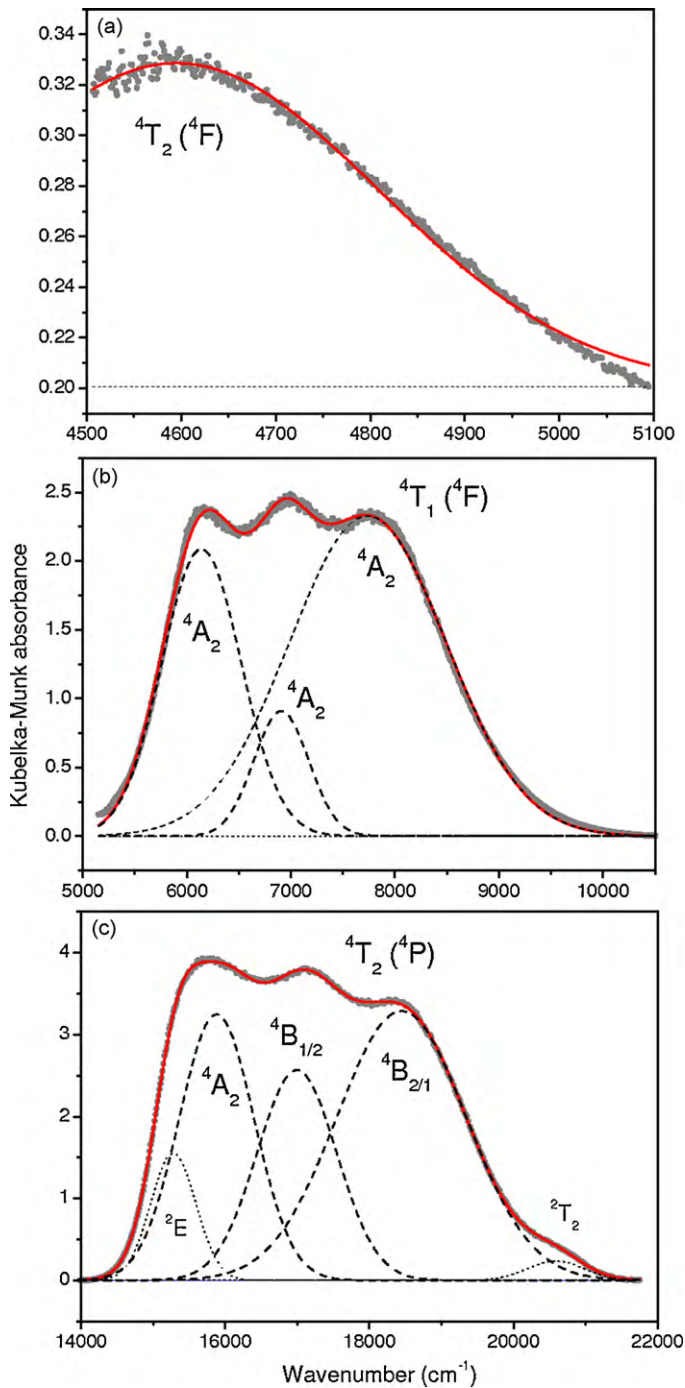
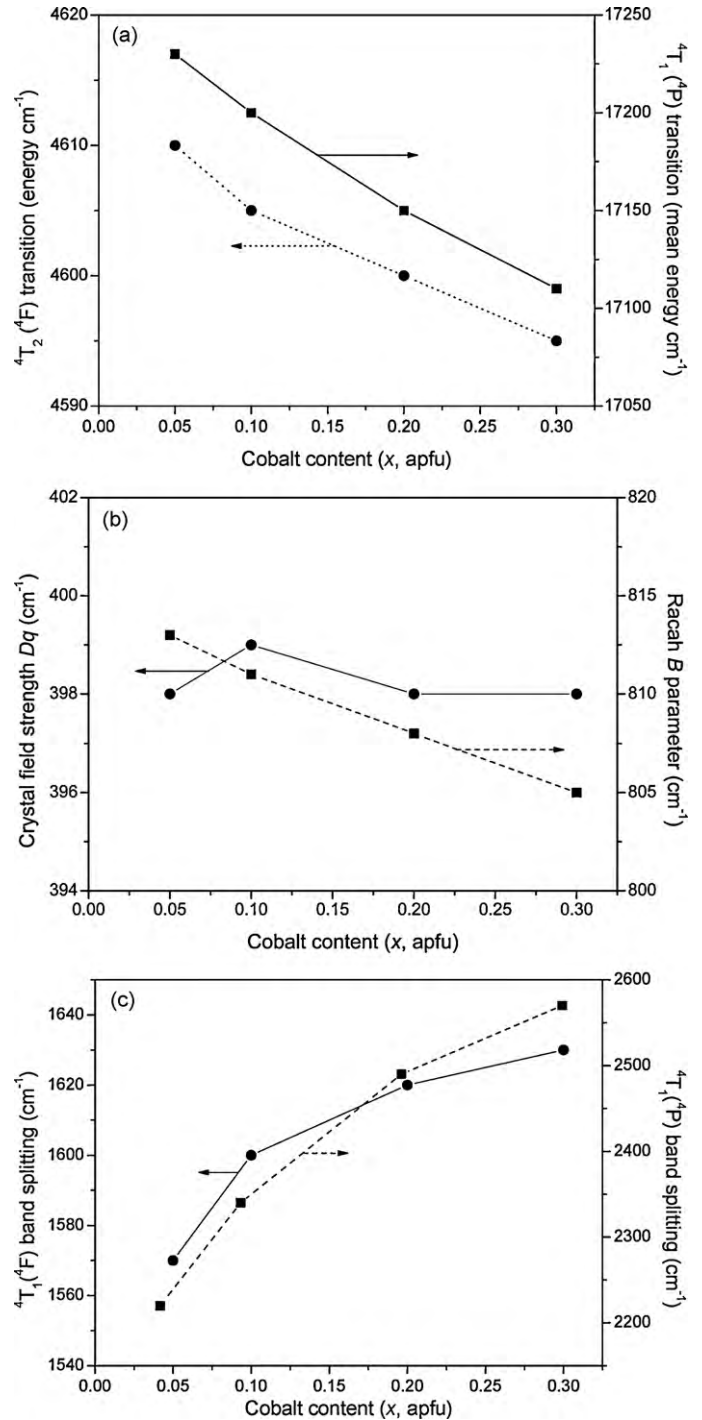Fig. 6. (a–c) Deconvolution of the optical spectra of willemite pigment W30.

Fig. 7. Optical parameters of willemite pigments as a function of the cobalt content: (a) energy of the Co^{2+} transitions; (b) crystal field strength Dq and interelectronic repulsion Racah B parameter; (c) Co^{2+} band splitting.

whether there is any reaction layer at the interface, since in STEM-HAADF the image intensity is approximately proportional to the square of the atomic number (Z^2),[31] which means that any chemical difference would create an atomic number contrast to chemically visualise diffusion layer formation at the interface (Fig. 11). As a result of the number of electrons inelastically scattered from higher atomic number elements, such as Co $(Z = 27)$ and Zn $(Z = 30)$, present in the pigment, the glass appears black coloured and willemite grey. From the STEM-HAADF image shown in Fig. 11(a), it can be deduced that no

diffusion layer is present at the interface. At this point, the question to be answered is whether there is any diffusion between glass and pigment or not. For this purpose, EDX analysis at STEM mode was performed due to the fact that the spatial resolution of this technique is around a few nanometres, so much better than EDX under SEM.[32] STEM-EDX line scan analysis confirms that the pigment composition contains only Co, Zn,
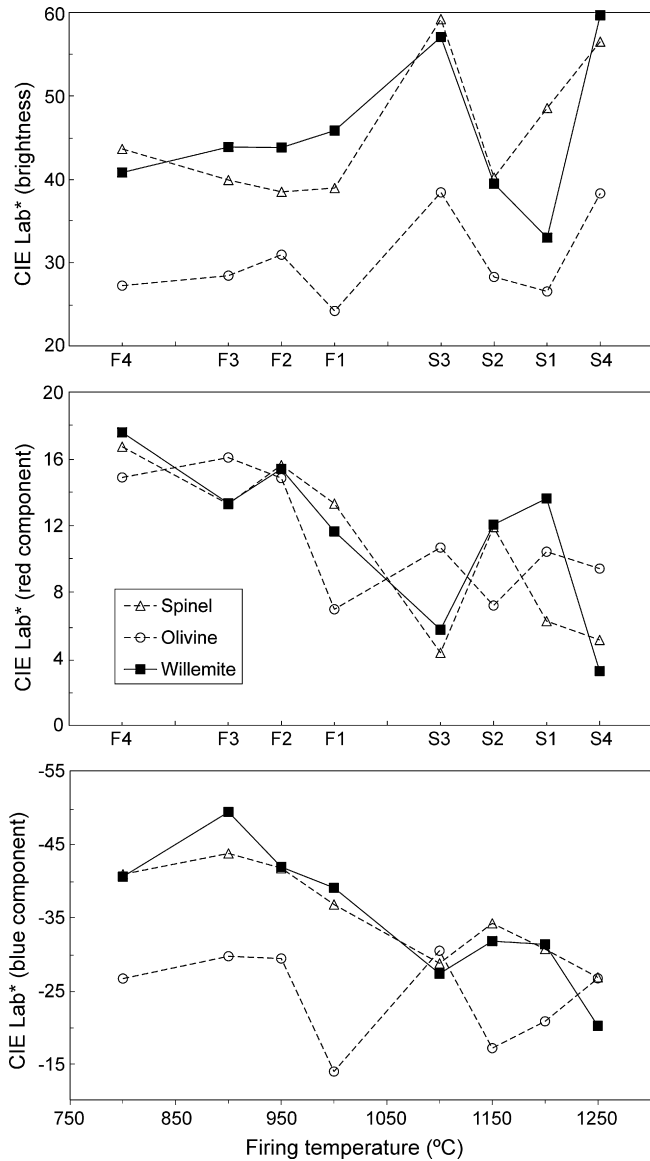
Fig. 8. Colour change vs. maximum firing temperature of pigments when used in different glassy coatings (F1–F4) and glazes (S1–S4).
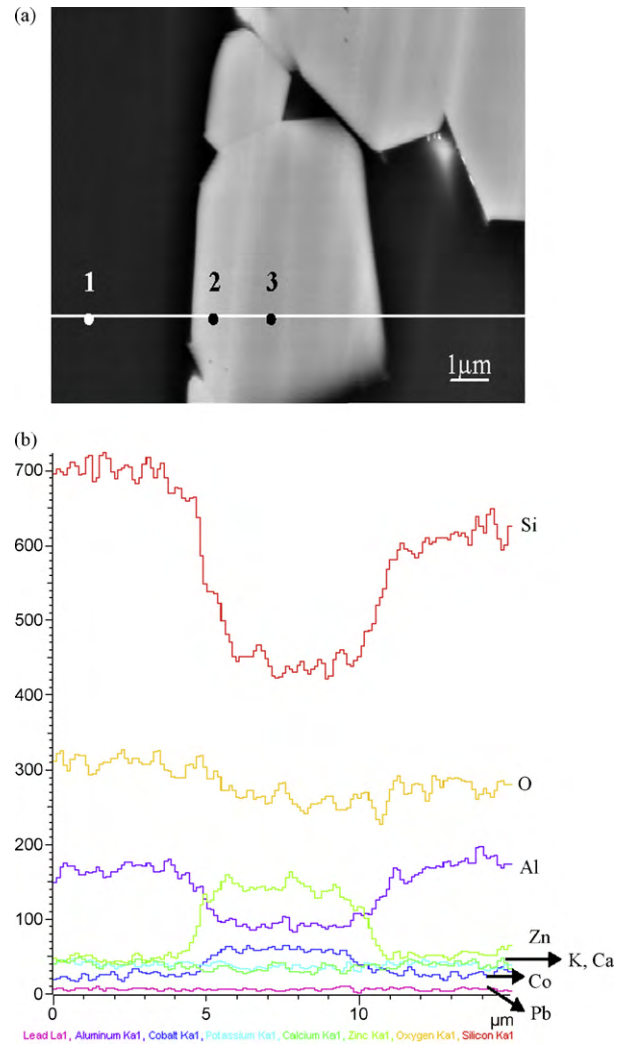

Fig. 9. (a) Backscattered SEM image of pigment grains embedded in the glassy coating and (b) line scan analysis of Al, Si, K, Ca, Zn, Co and Pb elements along the white line shown in (a).

Si, and O, while in the left hand side of Fig. 11(b) the intensity profiles of Co–K and Zn–K characteristic X-ray lines are almost zero up to a specific point (marked with A) plotting in the glass region, whereas going closer to the pigment grain a little increase of Co and Zn is observed. EDX spot analyses were acquired from glass and pigment (points 1 and 2 in Fig. 11(a)) and shown in Fig. 11(c) and (d), respectively. Comparing these line scans end point analysis, it can be deduced that no elements diffused and particularly Co and Zn did not migrate from the pigment to the glass.

Electron energy loss spectroscopy (EELS) was also applied to appraise if cobalt-doped willemite is chemically inert in contact with the glassy coating at 1050 °C. The spectrum acquired on the pigment (Fig. 12(a)) exhibits the Co-$L_{3,2}$ (779 and 794 eV) and Zn-$L_{3,2}$ (1020 and 1043 eV) edges along with O K edges; in contrast, the EEL analysis performed very close to the pigment grain neither Co nor Zn edges are visible (Fig. 12(b)). This con-
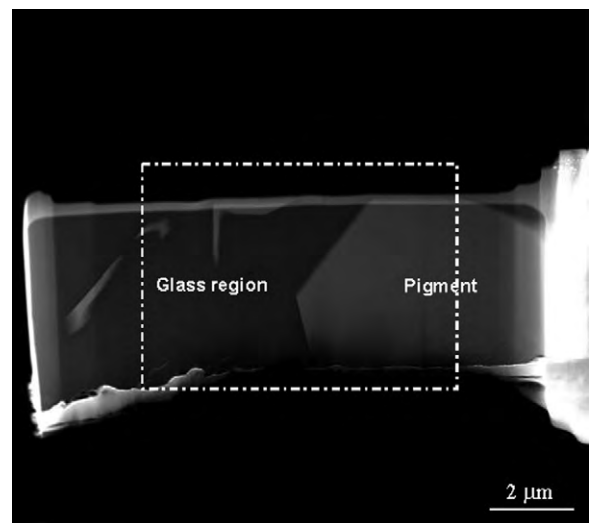

Fig. 10. Z-contrast STEM-HAADF image of FIB prepared sample showing a pigment grain in glassy coating at low magnification.
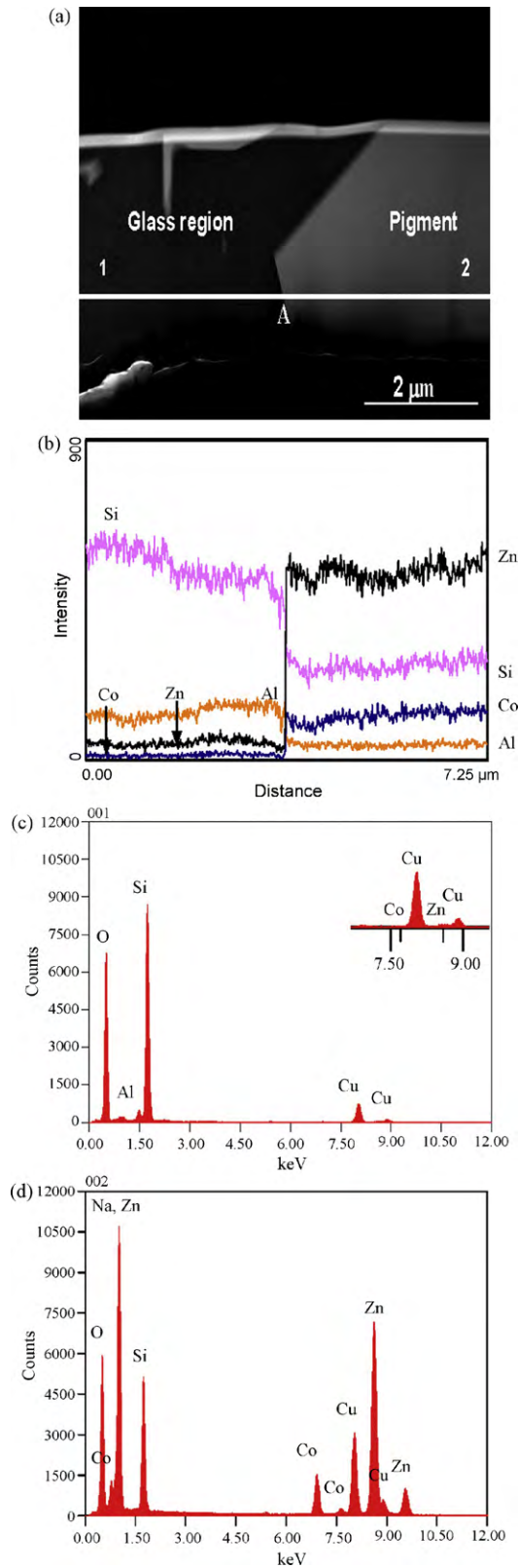
Fig. 11. (a) The STEM-HAADF image of pigment dispersed in glassy coating, magnified image of dashed rectangular area in Fig. 10, (b) STEM-EDX line scan analysis of Zn, Si, Co, Al elements along the white line shown in (a), (c) STEM-EDX spot analysis of glass region (point 1) and (d) pigment grain (point 2) shown in (a).
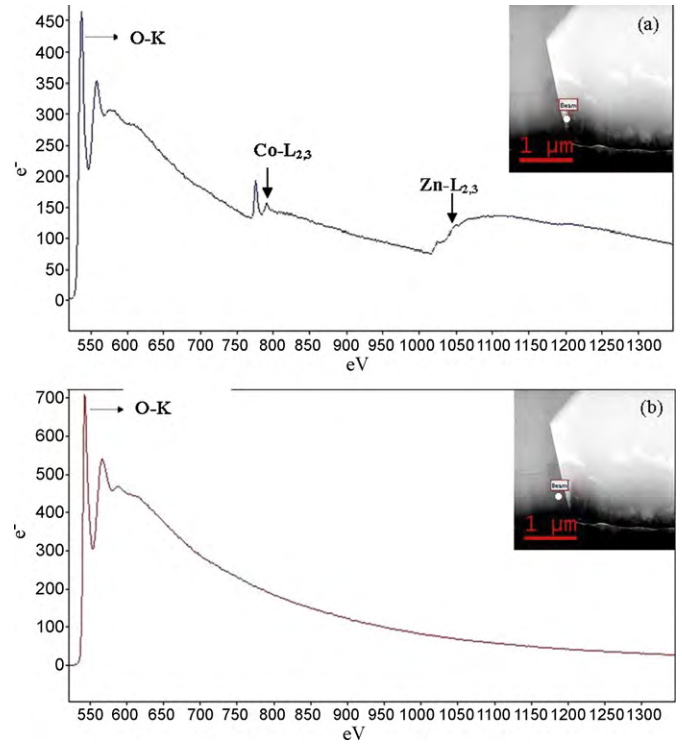

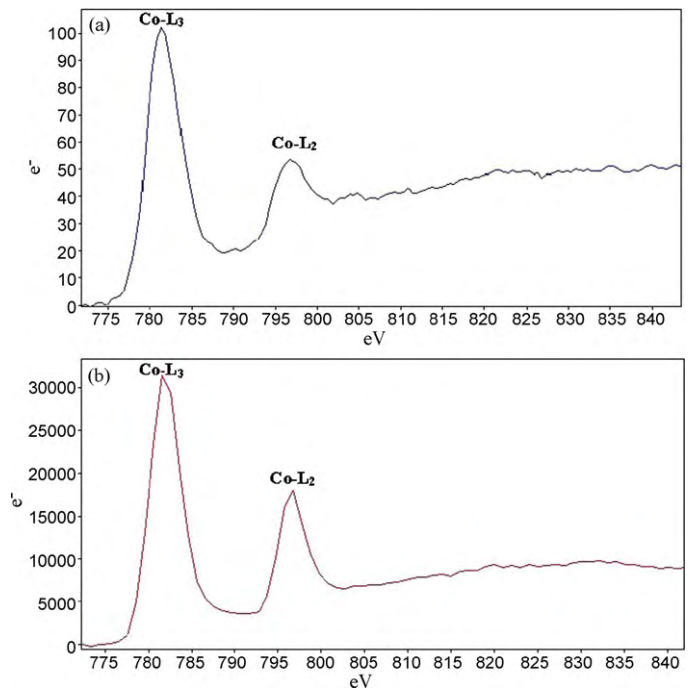Fig. 12. EEL spectra of (a) pigment, and (b) glassy coating in the 525–1350 eV energy loss rangef.

Fig. 13. The EEL spectra showing Co-L3,2 edges of (a) pigment grain and (b) reference CoO.

firms the STEM/EDX data in Fig. 11, leading to the conclusion that no diffusion layer is present at the pigment–glass interface, which means that the cobalt-doped willemite pigment produced in this work was chemically inert, at least at 1050 °C.

About the valence of Co ions in Zn_2SiO_4, a fingerprinting analysis was performed comparing the EEL spectra of the pigment and CoO taken as reference (Fig. 13). It can be appreciated that the energy of Co-L_3 and Co-L_2 edges is the same in both EEL spectra and the intensity ratio of the Co-L_3 to Co-L_2 is 1.76 ± 0.03 for the pigment and 1.75 ± 0.03 for CoO. Thus, the oxidation state of cobalt ion in the blue willemite pigment is Co(II+),[33,34] confirming the previous results on the Zn_2SiO_4 crystal structure obtained by using a different technique.[10]

4. Conclusions

Cobalt-doped willemite performs successfully as ceramic pigment, bestowing intense blue coloration on a wide range of glazes and glassy coatings. Thanks to its satisfactory chemical stability and optical features, willemite exhibits a colouring performance – comparing the same Co amount in the ceramic coating – better than conventional blue colorants, such as spinel $CoAl_2O_4$ or olivine Co_2SiO_4.

A detailed microstructural investigation – involving SEM-EDX, STEM-HAADF and TEM-EELS – supports technological tests, confirming that willemite pigments are chemically inert in contact with the ceramic matrix in which they are dispersed. No interface layer was formed and no diffusion phenomena were revealed between pigment and glassy coating at 1050 °C.

Cobalt incorporation in the willemite structure occurs with increasing unit-cell volume and parameters. Besides the ionic radius of Co^{2+} is smaller than that of the Zn^{2+} ion, cobalt doping causes an elongation of the mean metal–oxygen distance at the Zn1 site, which implies a preferential Co occupancy of this tetrahedral site. Growing the amount of cobalt induces an important change of the local symmetry of ligands – witnessed by the change of intertetrahedral tilting and TOT angles – confirmed by increasing splitting of Co^{2+} optical bands and spin-orbit coupling parameter. This enhances the distortion of tetrahedral site, which low point symmetry is likely to be the reason of the best optical properties of willemite with respect to cobalt aluminate spinel and cobalt silicate.

A deeper understanding of properties and behaviour of Co-doped willemite is gained from these insights which, on one side, prove that high quality pigments can be actually obtained using secondary precursors, e.g. ZnO recovered from slag, and on the other side that $(Zn,Co)SiO_4$ does is a promising pigment for novel ceramic applications, particularly new decoration techniques.[35,36]

Acknowledgements

References

1. Bragg WL, Zachariasen WH. The crystalline structure of phenakite, Be_2SiO_4, and willemite, Zn_2SiO_4. Z Kristallogr 1930;**72**:518–28.
2. Hang C, Simonov MA, Belov NV. Crystal structures of willemite $Zn_2[SiO_4]$ and its germanium analog $Zn_2[GeO_4]$. Sov Phys Crystallogr 1970;**15**:387–90.
3. Klaska K-H, Eck JC, Pohl D. New investigation of willemite. Acta Cryst 1978;**B34**:3324–5.
4. McMurdie H, Morris M, Evans E, Paretzkin B, Wong-Ng W, Hubbard C. Standard X-ray diffraction powder patterns from the JCPDS research associationship. Powder Diffr 1986;**1**:265–75.
5. Van Der Kolk E, Dorenbos P, Van Eijk CWE, Bechtel H, Jüstel T, Nikol H, et al. Optimised co-activated willemite phosphors for application in plasma display panels. J Lumin 2000;**87–89**:1246–9.
6. Ahmadi TS, Haase M, Weller H. Low-temperature synthesis of pure and Mn-doped willemite phosphor (Zn_2SiO_4:Mn) in aqueous medium. Mater Res Bull 2000;**35**:1869–79.
7. Sreekanth Chakradhar RP, Nagabhushana BM, Chandrappa GT, Ramesh KP, Rao JL. Solution combustion derived nanocrystalline Zn_2SiO_4:Mn phosphors: a spectroscopic view. J Chem Phys 2004;**121**:10250–9.
8. Wan J, Wang Z, Chen X, Mu L, Yu W, Qian Y. Controlled synthesis and relationship between luminescent properties and shape/crystal structure of Zn_2SiO_4:Mn^{2+} phosphor. J Lumin 2006;**121**:32–8.
9. Yan B, Huang H. Matrix-inducing synthesis and luminescence of Zn_2SiO_4:xTb^{3+} submicrometer phosphors derived from the sol–gel assembling of different multicomponent hybrid precursors. J Alloys Compd 2007;**429**:338–42.
10. Brunold TC, Güdel HU, Cavalli E. Absorption and luminescence spectroscopy of Zn_2SiO_4 willemite crystals doped with Co^{2+}. Chem Phys Lett 1996;**252**:112–20.
11. Rudkovskaya NV, Mikhailenko NY, Lisinenkova SB, Levin YM. Diffusion processes in firing willemite glaze on quartz glass ceramics. Glass Ceram 2003;**60**:226–8.
12. Hu AM, Li M, Mao Dali DL, Liang KM. Crystallization and properties of a spodumene-willemite glass ceramic. Thermochim Acta 2005;**437**:110–3.
13. Ohsato H. Research and development of microwave dielectric ceramics for wireless communications. J Ceram Soc Jpn 2005;**113**:703–11.
14. Chandrappa GT, Ghosh S, Patil KC. Synthesis and properties of willemite. Zn_2SiO_4, and M^{2+}:Zn_2SiO_4 (M = Co and Ni). J Mater Synth Process 1999;**7**:273–9.
15. Forés A, Llusar M, Badenes JA, Calbo J, Tena MA, Monrós G. Cobalt minimisation in willemite ($Co_xZn_{2-x}SiO_4$) ceramic pigments. Green Chem 2000;**2**:93–100.
16. Llusar M, Forés A, Badenes JA, Calbo J, Tena MA, Monrós G. Color analysis of some cobalt-based blue pigments. J Eur Ceram Soc 2001;**21**:1121–30.
17. Larson AC, Von Dreele RB. GSAS, general structure analysis system. Los Alamos: Laur, Los Alamos National Laboratory; 1988.
18. Toby BH. EXPGUI, a graphical user interface for GSAS. J Appl Crystallogr 2001;**34**:210–3.
19. Swanson DK, Peterson RC. Polyhedral volume calculation. Can Miner 1980;**18**:153–6.
20. Marfunin AS. Physics of minerals and inorganic materials. Berlin: Springer; 1979.
21. Torres FJ, Rodríguez-Mendoza UR, Lavín V, Ruiz de Sola E, Alarcón J. Evolution of the structural and optical properties from cobalt cordierite glass to glass–ceramic based on spinel crystalline phase materials. J Non-Cryst Solids 2007;**353**:4093–101.
22. Lever ABP. Inorganic electronic spectroscopy. Amsterdam: Elsevier; 1984.
23. Matteucci F, Lepri Neto C, Dondi M, Cruciani G, Baldi G, Boschi AO. Colour development of red perovskite pigment Y(Al, Cr)O_3 in various ceramic applications. Adv Appl Ceram 2006;**105**:99–106.

24. Tenorio Cavalcante PM, Dondi M, Guarini G, Barros FM, da Luz AB. Ceramic application of mica titania pearlescent pigments. *Dyes Pigments* 2007;**74**:1–8.

25. Thomas PJ, Midgley PA. An introduction to energy-filtered transmission electron microscopy. *Top Catal* 2002;**21**:109–38.

26. Louisnathan SJ. Refinement of the crystal structure of hardystonite, $Ca_2ZnSi_2O_7$. *Z Kristallogr* 1969;**130**:427–37.

27. Ericsson T, Filippidis A. Cation ordering in the limited solid solution Fe_2SiO_4–Zn_2SiO_4. *Am Miner* 1986;**71**:1502–9.

28. Krause MK, Sonntag R, Kleint CA, Rönsch E, Stüsser N. Magnetism and cation distribution in iron zinc silicates. *Physica B* 1995;**213–214**:230–2.

29. Duan X, Yuan D, Cheng X, Sun Z, Sun H, Xu D, et al. Spectroscopic properties of Co^{2+}:$ZnAl_2O_4$ nanocrystals in sol–gel derived glass–ceramics. *J Phys Chem Solids* 2003;**64**:1021–5.

30. Kyser DF, Murata K. Quantitative electron microprobe analysis of thin films on substrates. *IBM J Res Dev* 1974;**18**:352–63.

31. Varela M, Lupini AR, Van Benthem K, Borisevich AY, Chisholm MF, Shibata N, et al. Materials characterization in the aberration-corrected scanning transmission electron microscope. *Annu Rev Mater Res* 2005;**35**:539–69.

32. Williams DB, Watanabe M, Papworth AJ, Li JC. Quantitative characterization of the composition, thickness and orientation of thin films in the analytical electron microscope. *Thin Solid Films* 2003;**424**:50–5.

33. Wang ZL, Yin JS, Jiang YD. EELS analysis of cation valence states and oxygen vacancies in magnetic oxides. *Micron* 2000;**31**:571–80.

34. Yu-Zhang K, Imhoff D, Leprince-Wang Y, Roy E, Zhou SM, Chien CL. Multiscale analysis of the nanostructured granular solid CoO–Ag by TEM and EELS. *Acta Mater* 2003;**51**:1157–66.

35. Gardini D, Dondi M, Costa AL, Matteucci F, Blosi M, Galassi C, et al. Nano-sized ceramic inks for drop-on-demand ink-jet printing in quadrichromy. *J Nanosci Nanotechnol* 2008;**8**:1979–88.

36. Cavalcante PMT, Dondi M, Guarini G, Raimondo M, Baldi G. Colour performance of ceramic nano-pigments. *Dyes Pigments* 2009;**80**:226–32.